WILEY-VCH

Cyclometalated Iridium (III) Complex as Microtubule Probe for Correlative Super-Resolution Fluorescence and Electron Microscopy

Xiaohe Tian[1,2,3,4], Cesare De Pace[4,5,6], Lorena Ruiz-Perez[4,5,6], Bo Chen[7], Rina Su[1], Mingzhu Zhang[2], Ruilong Zhang[2], Qiong Zhang[2], Qin Wang[8], Hongping Zhou[2], Jieying Wu[2], Zhongping Zhang[2,3,9,*] Yupeng Tian[2,*], and Giuseppe Battaglia[2,3,5,6,10,11,*]

[1] *School of Life Science, Anhui University, Hefei, P. R. China*

[2] *Department of Chemistry, Anhui University, Hefei, P. R. China*

[3] *Institute of Physical Science and Information Technology, Anhui University, Hefei, P. R. China*

[4] *Department of Chemistry, University College London, London, United Kingdom*

[5] *Institute for the Physics of Living Systems, University College London, London, United Kingdom*

[6] *EPSRC/JEOL Centre for Liquid Phase Electron Microscopy, University College London, University College London*

[7] *School of Materials Science and Engineering, Tongji University, Shanghai 201804, China*

[8] *Biotechnology Centre, Anhui Agriculture University, Hefei 230036, China*

[9] *CAS Center for Excellence in Nanoscience, Institute of Intelligent Machines, Chinese Academy of Science, Hefei, China*

[10] *Institute for Bioengineering of Catalonia, The Barcelona Institute for Science and Technology (BIST), Barcelona, Spain.*

[11] *Catalan Institution for Research and Advanced Studies, Barcelona, Spain*

*Corresponding authors: Prof Zhongping Zhang Email: zpzhang@iim.ac.cn; Prof Yupeng Tian Email: yptian@ahu.edu.cn; and Prof Giuseppe Battaglia Email: g. battaglia@ucl.ac.uk.

Abstract

The visualization of microtubules by combining optical and electron microscopic techniques provides valuable information to understand correlated intracellular activities. However, the lack of appropriate probes to bridge both microscopic resolutions restricts the

areas and structures that can be comprehended within such highly assembled structures. Here, a versatile cyclometalated Iridium (III) complex was designed that achieves synchronous fluorescence-electron microscopy correlation for the first time. The selective insertion of the probe into microtubule triggers remarkable fluorescent enhancement along with promising electron contrast. The long-life, highly photostable probe allows live-cell super-resolution imaging of tubulin localization and motion with a resolution of ~ 30 nm. Furthermore, correlative light-electron microscopy and energy-filtered transmission electron microscopy reveals the well-associated optical and electron signal at a high specificity, with interspace of ~ 41Å of microtubule monomer in cells.

1. Introduction

The structure of living cells involves a complex and highly dynamic assembly of proteins, lipids and nucleic acids. Imaging techniques such as electron and optical microscopy provide both structural and dynamic information to dissect cellular complexity. Currently, there are tools such as x-ray crystallography and transmission electron microscopy (TEM) [1] that resolve structures of individual cell components at atomic resolution. However, the new frontier of structural cell biology is a holistic characterization of cellular units and how their structures adapt to the very crowded and complex cell environments. [2] Techniques such as cryo-electron tomography [3] provide a glimpse of how cellular components operate over multiple length-scales. New sample holders enable TEM visualization of wet samples and whole cells. [4] However, TEM does not use probes that enable molecular specificity and often suffer from a limited observation window. In contrast, optical microscopy is the workhorse of cell biology because this technique can be combined with selective molecular probes such as fluorescent proteins, immune-labelling, and synthetic dyes to image live specimens across several dimensions. [5] In particular, in the last two decades super-resolution optical microscopy (SRM) techniques such as stimulated emission depletion (STED) and stochastic optical reconstruction microscopy (STORM) have improved optical microscopy resolution[6] to tens of nm, which is

close to the resolution of TEM. However, the quality of SRM imaging is probe-dependent, and resolution limitation is defined by the probe own size. Besides, most SRM techniques require photostability, and, for STORM, photo-switchable, fluorescent probes, [5, 7] thereby hampering time resolution measurements. These issues limit the scale that SRM can access to reveal molecular arrangements of cellular components, [8, 9] thereby bridging structure with function. To circumvent SRM and TEM limitations involves combining them to capture a multidimensional and correlated image that contains high resolution dynamic structural information alongside functionality, cellular localization and possibly chemical mapping. [9, 10]

Correlative light electron microscopy (CLEM) [11] is fast becoming a critical tool to study biology to overcome the above barriers. However, this calls for an entirely new way of designing functional materials that possess both the adequate photo-physical properties for SRM while providing sufficient density to enhance contrast in electron microscopy. [10] Among the different chemistries, compounds containing at least one metal-to-carbon bond, known collectively as organometallic molecules, are extremely promising compounds for CLEM. [12] We have shown that metal complexes can be used in electron or optical microscopy to image nuclear DNA, [13] mitochondrial DNA, [14] lipid membranes [15] and nuclear factor kappa B. [16] This shed light to utilize such materials to correlate light and electron information.

In this work, the rational design of cyclometalated iridium (III) complexes (cIr-Tub, cIr-1 ad cIr-2) and their application in correlative optical and electron microscopy are presented. We chose the microtubule as the subcellular target since it represents a major component of all eukaryotic cytoskeleton that consisted by α- and β-tubulin dimers, catalyzed by GTP binding and polymerized into microtubules. [17] Above all, intracellular microtubules CLEM imaging using a single agent had not previously achieved elsewhere. It is known that Iridium (III) complexes are ideal luminescent materials with a tunable MLCT (metal-to-ligand charge transfer) emissive from blue to red, with high photostability, and a large stock-shift. [22, 23] Taking advantage of these features, we showed the obtained cIr-Tub complex displayed red

emissions upon selectively binding microtubule in live cells. *In cellulo* and *ex vivo* super-resolution imaging demonstrated significantly improved resolution due to cIr-Tub long-life and photostable nature. Mostly importantly, we indicated such complex target microtubules offered high contrast in electron microscopy at molecular level under EF-TEM, and enabled for the first time the correlation of super-resolution and electron microscopy under CLEM with high specificity.
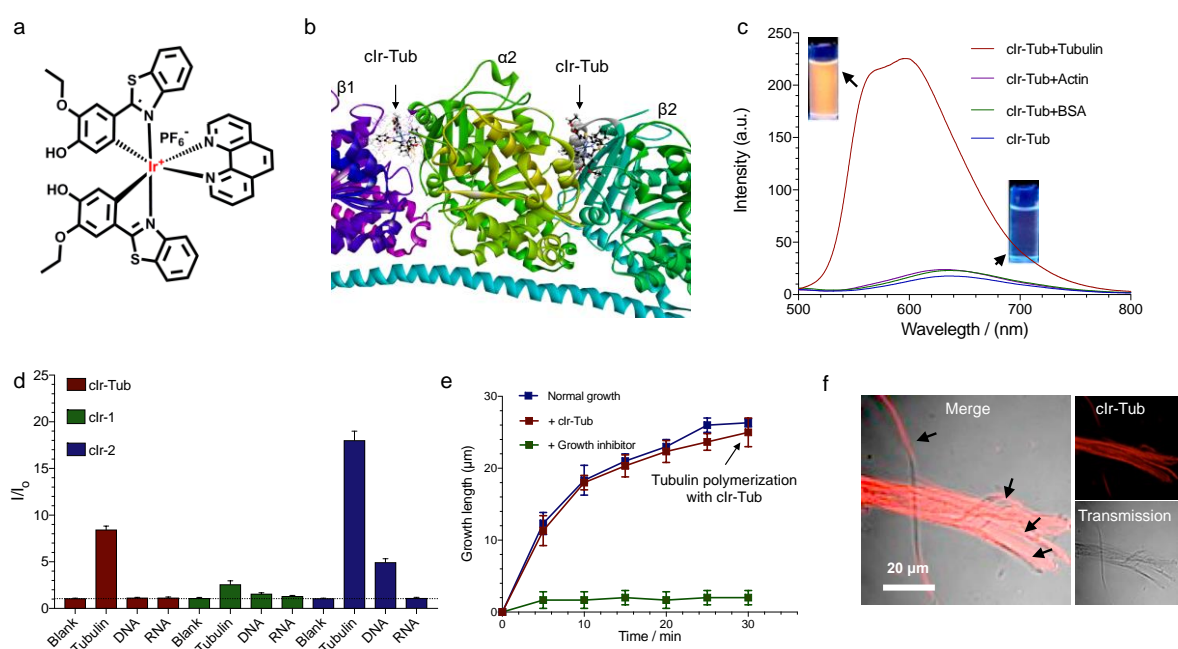
2. Results and discussion

Figure 1: In vitro assessment of microtubules binding with cIr-Tub complex. The chemical structure of cIr-Tub Ir complex (cIr-Tub) (a). Computer modelling of Ir-Tub complex (b) docking into αβ and βα tubulin binding sites. Emission spectra of cIr-Tub complex (10 μM) bound to tubulin, actin and bovine serum albumin (all concentration = 36 μg/mL). The inserts show the corresponding cuvette of cIr-Tub and cIr-Tub + tubulin solution under UV irradiation (c). Normalised fluorescence intensity of (d) free (blank) cIr-Tub, cIr-1 and cIr-2 and the corresponding signal when bound to tubulin (30 μg/mL), dsDNA (10 μM), and RNA (10 μg/mL) respectively. In vitro polymerisation of tubulin protein into microtubules (e) in the presence of growth inhibitor (Nocodazole) and (f) cIr-Tub with its correspondence florescent images. The arrows indicated microtubule fibers.

We synthesized the cIr-complexes (**Fig. 1**a) and two similar complexes (cIr-Tub and cIr-1,

cIr-2, Figure S1, CCDC number: 2001309, 2002391 and 2002390) using vanillin and phenanthroline to coordinate the electron-dense Ir(III), obtained complexes with Ir-N and Ir-C bonds that possess high stability and photo resistance. Vanillin is a food additive with minimal cytotoxicity towards living systems that forms thiazole derivatives by carboxylation with *o*-aminothiophenol, resulting in larger conjugated systems and push-pull electronic groups. Phenanthroline is a classic coordination group with a planar conjugated system that enables yellow emission upon iridium binding. [22] Such properties bestow the complex with longer lifetimes when compared with that of conventional organic fluorophores and, most relevant here, offer the capability for time-gated STED, resulting in improved imaging resolution.[8] Finally, thiazole derivatives and phenanthroline allow for hydrogen bonding and hydrophobic interactions (π–π and π-alkyl) with protein amino acid residues, which restrains the molecular torsion of the extended conjugated systems to augment complex fluorescence and consequently enable the "light switch" phenomenon.

The synthesis and characterization of the Ir (III) phenanthroline complex cIr-Tub and its analogous complexes cIr-1 and cIr-2 are provided in the Supporting Information. The final product was crystallized (Figure S2 and Table S1) and characterized by ^{13}C NMR (Figure S3), ^{1}H NMR (Figure S4) and mass spectroscopy (Figure S5). The fluorescence spectrum of clr-Tub exhibits a weak red broad emission from 520 to 700 nm (Figure S6), [24] with a large Stocks-shift (118 nm) [25] and lifetimes on the order of 20 ns (Table S2).

The binding of cIr-Tub to tubulin was first evaluated *in silico* via molecular docking using the Discover Studio ligand fit Vina software (version 2016, The Biovia Co) and the protein data base (PDB) tubulin heterodimer structure (PDB ID: 5J2T). [26] This particular structure mimics the structural rigidity of tubulin within microtubules and has a size that is computationally manageable. We set two tubulin dimers as the minimal units of receptor microtubules for cIr-Tub and present the resulting complex in **Figure. 1**b, Figure S7 and Figure S8 (Video S1 – S4). We found that the Ir(III) complex binds to both tubulin αβ and βα sites in the same site as

vinblastine (Table S3), a well-known tubulin-targeting anticancer drug. [27] It is also indicated that cIr-Tub complex and vinblastine share many similarities such as volume and molecular weight (Figure S9). We demonstrated that cIr-Tub could interacts with several residues including Phe214, Asn329, Pro325, Val353, Leu248, Val250, Tyr224, Leu227 and Tyr210 via π-π and π-alkyl interactions as well as forming a hydrogen bond network that is mapped in Figure S7. The interaction is relatively strong, with much higher calculated binding energy than that of vinblastine (Table S3).

We further confirmed the interaction experimentally by fluorescence spectroscopy and observed that cIr-Tub fluorescence is enhanced when the probe is bound to tubulin (**Figure 1**c). The titration experiments (Figure S10) and polyacrylamide gel electrophoresis of tubulin (55 kDa) after staining with cIr-Tub (Figure S11) revealed that both effects are tubulin-concentration dependent. It is also showed that the interaction of cIr-Tub against tubulin is very specific, without responding to other various biomolecules (**Figure 1**d and Figure S12).

In Table S2, we report the measured photo-physical properties of cIr-Tub fluorescence in different solvents and when bound to tubulin. The data showed that interaction is likely to be driven by the phenanthroline ligands as demonstrated with other metal complexes. [13, 28] We monitored tubulin polymerization *in vitro* at 37 °C to fully assess the suitability of cIr-Tub as a probe. The results report tubulin growth into microtubules as measured by optical microscopy, and the inhibitor nocodazole (500 nM) was used as a control. [29] After 30 min, nocodazole prevented tubulin polymerization, while cIr-Tub did not alter microtubule growth(**Figure 1**e) and gave the desired light switch effect (**Figure 1**f).

Next, we investigated the application of the cIr-Tub complex *in vivo* and measured cytotoxicity by incubating the cIr-Tub complex with several types of cells, including immortalized cancerous cells (A549, HeLa, MCF-7, HepG2 and HEK) as well as primary human dermal fibroblasts (HDF) and human embryo liver fibroblasts (HELF). Incubation of clr-Tub with these cells showed a minimal effect on cell viability over 72 h, indicating that the

probe does not affect cell metabolic activity (Figure S13). Upon treatment of living cells with cIr-Tub (Stock solution 1mM in DMSO, then diluted into working concentration), the intracellular microtubules emitted a strong red fluorescence signal under excitation at 450 nm. The *in-situ* emission spectra were recorded under the lambda model and fitted with *in vitro* spectra in solution for a range of wavelengths (Figure S14).

Co-staining experiments were consequently performed using the tubulin probes SiR-Tubulin (**Figure 2**a) in live cells. Furthermore, an α-tubulin antibody (**Figure 2**b) demonstrated a high degree of colocalization with the cIr-Tub probe and microtubules in fixed cells. Microtubule selectivity was also demonstrated by the lack of colocalization with other subcellular components including mitochondria, endoplasmic reticulum, lysosomes and actin (Figure S15). In contrast, cIr-Tub analogues, cIr-1 displayed a much weaker emission than clr-Tub, whereas cIr-2 showed non-specific nuclear targeting (Figure S16).

Interestingly, the cIr-Tub probe was very efficient in monitoring the structure of microtubules dynamics (Figure S17) also during mitosis (**Figure 2**c). HepG2 cells were co-stained with nuclear dye, Nuc-Red, which allowed negligible signal overlap and highlighted the transformation from chromatin to chromosomes (prometaphase), indicating the progression of cell division. cIr-Tub enabled visualization of microtubule polymerization through the centriole (prophase) to mitotic spindles (metaphase). Structural and numeric aberrations (excess centrosomes) can be observed commonly in human tumors. [30] Hence the ability of cIr-Tub to effectively monitor microtubules dynamically during mitosis provides an attractive approach to investigate cancer biology.
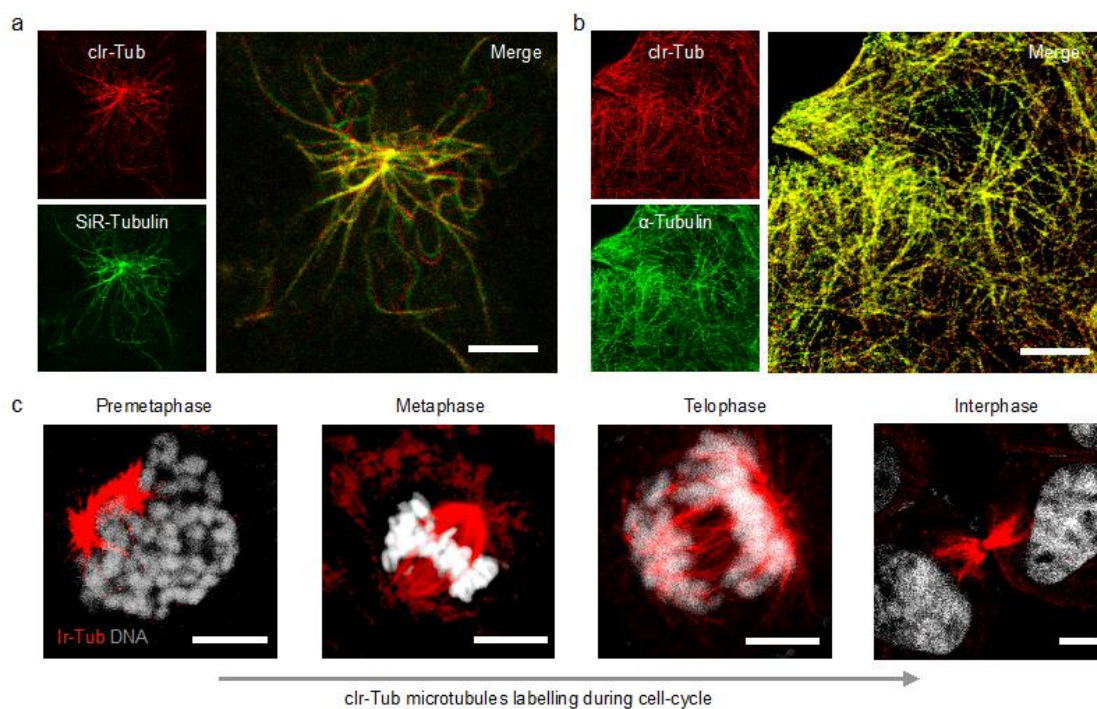
Figure 2: In cella assessment of cIr-Tub complex for microtubules staining. *Confocal laser scanning micrographs of live HepG2 cells (a) incubated with 5μg/mL cIr-Tub for 30 min and co-stained with SiR-Tubulin (λ_{Ex} = 640 nm, λ_{Em} = 670 nm). Confocal laser scanning micrographs of fixed HepG2 cells (b) incubated with 5 μM cIr-Tub for 30min and immunofluorescently labeled with β-Tubulin antibody (secondary: λ_{Ex} = 488 nm, λ_{Em}= 520-550 nm) Scale bar = 5 μm. Snapshots of dividing cells at different cell cycle phase (c) stained with cIr-Tub (5μM) and with DNA dye NucRed (λ_{Ex} = 633 nm, λ_{Em} = 650-700 nm). Scale bar = 5 μm*

Encouraged by the above results, we further assessed the capabilities of cIr-Tub to mark microtubules *ex vivo* and its use in STED microscopy. Photo-bleaching experiments suggested that the fluorescence signal was preserved after 400 scans during either the confocal or STED mode (Figure S18), indicating a superior light resistance when compared with that of reported microtubule marker (e.g., SiR-tubulin) or other commercial available dyes (e.g. Alex Fluor 488, Figure S19).

We expected the cIr-Tub iridium metalcore to be considerably resistive to the high laser power associated with STED imaging and hence enable high-resolution imaging. As shown in **Figure 3**a and its corresponding cell imaging (**Figure 3**b), the cIr-Tub labelled microtubules (5

μM cIr-Tub, fixed HepG2 cells) full width at half maximum (FWHM) decreases with increasing STED laser power intensity or gating time (ns). At full power and longest gating time, we can image with a resolution as low as 30 nm, and with 10% STED laser power and 20 ns gated time we can image as low as 50 nm.

Such an augmented resolution is a critical factor when imaging sensitive samples such as the microtubule-rich brain tissues presented in **Figure 3**c. Here, STED imaging highlights the elongated fibril structures throughout the hippocampus region and collection of over 150 optical slides, which allows visualization of the microtubule networks in 3D (**Figure 3**d). This imaging approach enabled the visualization of complex neuronal microtubular networks. In addition, some ultra-structures have been captured and might well correspond to neuronal subunits, including the growth cone, nascent neurites and spines with high spatial resolution (**Figure 3**e). However, further immune labelling should be performed in order to confirm these structures.
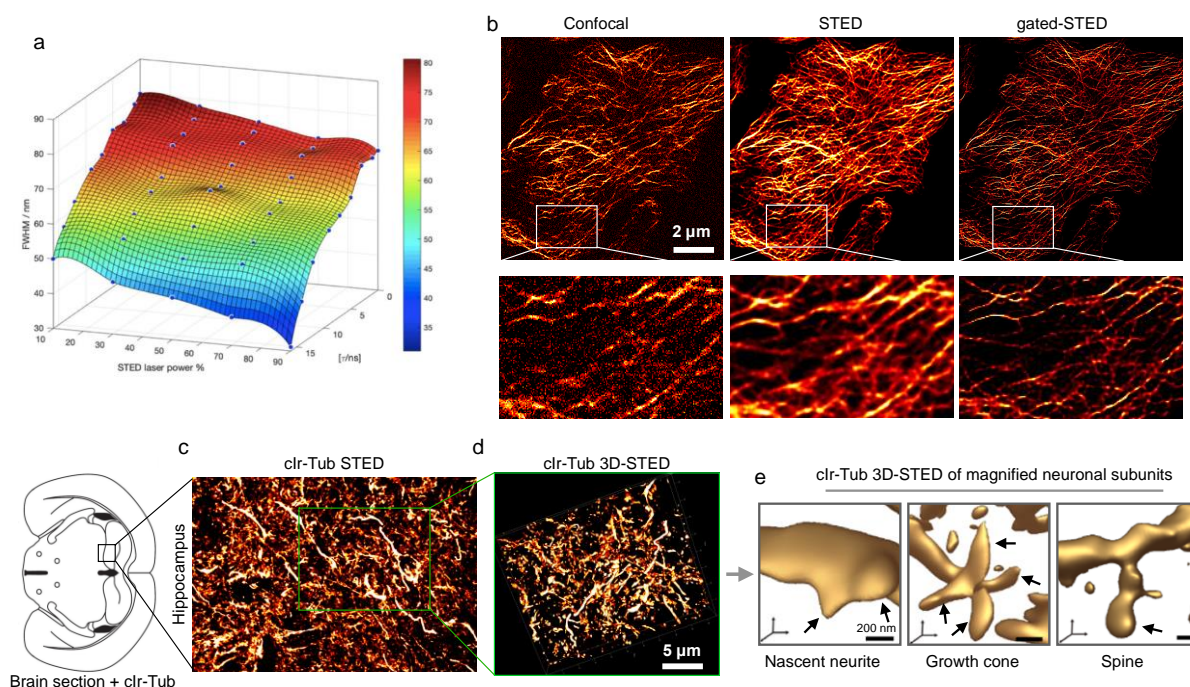

Figure 3: Feasibility of Ir-Tub complex for STED microscopy. *HepG2 cell fixed and stained with 5μM Ir-Tub, showing the Ir-Tub labeled microtubules resolution indicated by (a) full width at half maximum (FWHM) as a function of the STED laser power intensity (donuts laser = 592 nm, full power = 12 mW) and gating time (ns). Corresponding micrographs (b) by confocal, STED (full power) and time gated-STED (15ns)*

microscopy. Graph (c) STED micrographs of brain hippocampus sections labeled with cIr-Tub complex (d)
and its 3D rendering of STED micrographs (e) and magnified regions showing neuronal subunits (indicated
by arrows).

We finally exploited if cIr-Tub could provide selective contrast for electron microscopy and eventually bridge optical-electronic information. Initially, this was tested by pretreating cells with cIr-Tub, post-fixed by osmium tetroxide (OsO_4), a specific membrane structure stains for transmission electron microscopy. The control group solely treated with OsO_4 solely displayed clear membrane structure including vesicles, endoplasmic reticulum and mitochondria; however, microtubule structures were not visible (Figure S20). For comparison, cells treated with both stains, cIr-Tub and OsO_4 showed interesting complex networks where the microtubules (stained by cIr-Tub) appear to interact intimately mitochondrial membrane structure (stained by OsO_4); Cells solely treated cIr-Tub indicated microtubules were clearly visible with high selectivity. Although other staining agents such as uranyl acetate (UA) or lead citrate (LC) can also stain microtubules at high concentration, these approaches also displayed clear unspecific staining. [31] The comparison between cIr-Tub and UA/LC staining demonstrates that the image contrast afforded by cIr-Tub provides better resolution of the microtubules and also a contrast enhancement when compared with that of UA/LC staining (Figure S21).

The above results validated cIr-Tub for an unprecedented combination of imaging modalities, providing microtubule-selective contrast for both super-resolution optical microscopy and electron microscopy. Thus, cIr-Tub treated cells were imaged using CLEM by sequential super-resolution microscopy (airy-scan model) followed by STEM. As shown in **Figure 4**a, the microtubule network was visible under both optical and electron microscopic channel with the two signals overlapping with a colocalization Pearson coefficient of Rr = 0.91, confirming cIr-Tub affinity towards tubulin and showing its suitability for CLEM imaging.

To prove cIr-Tub is associated with microtubules at the molecular level, cell sections were imaged via energy-filtered TEM (EF-TEM). Such an imaging mode allows chemical mapping and hence the position of the iridium atoms within the microtubule structures by selecting electrons that have lost a specific amount of energy from inelastic scattering interactions with the inner-shell ionization. In the present study, the iridium O shell maps were acquired alongside conventional TEM imaging. In **Figure 4**b the details of a single microtubule structure are shown both in conventional (unfiltered) TEM and EF-TEM, a merged image showing the Iridium elemental distribution along with the microtubule structures with sub-nanometer resolution. The distances between neighboring iridium atoms obtained from the elemental map were measured (**Figure 4**c), showing that the probes were distributed along with the microtubule structure with average interspaces of 4.1±0.3 nm. The distance between each Iridium element might match with value calculated in the reconstructed microtubule model in **Figure 4**d (and Figure S22). However, it is important to point out while we detect Iridium both alone (Fig S22a) and mixed with a polymer (Fig.S22b) using EF-TEM, the technique is extremely sensitive to the specimen thickness with large mean free path (mfp) hindering the filtering process (see Fig S22a). We thus scan the cell section for the shortest mfp (see Fig.S23) to than image the region of interest for Iridium. Although metallic complexes (e.g. Iridium) with high atomic number offers better scattering performance, we believe further investigation would be necessary and indeed ongoing in our lab. Nonetheless, all the above results suggested that the cIr-Tub complex is internalized effectively within intracellular microtubules and capable of acting as a multifunctional probe for light (confocal, STED and time-gated STED) and electron microscopy (TEM, STEM and EF-TEM).
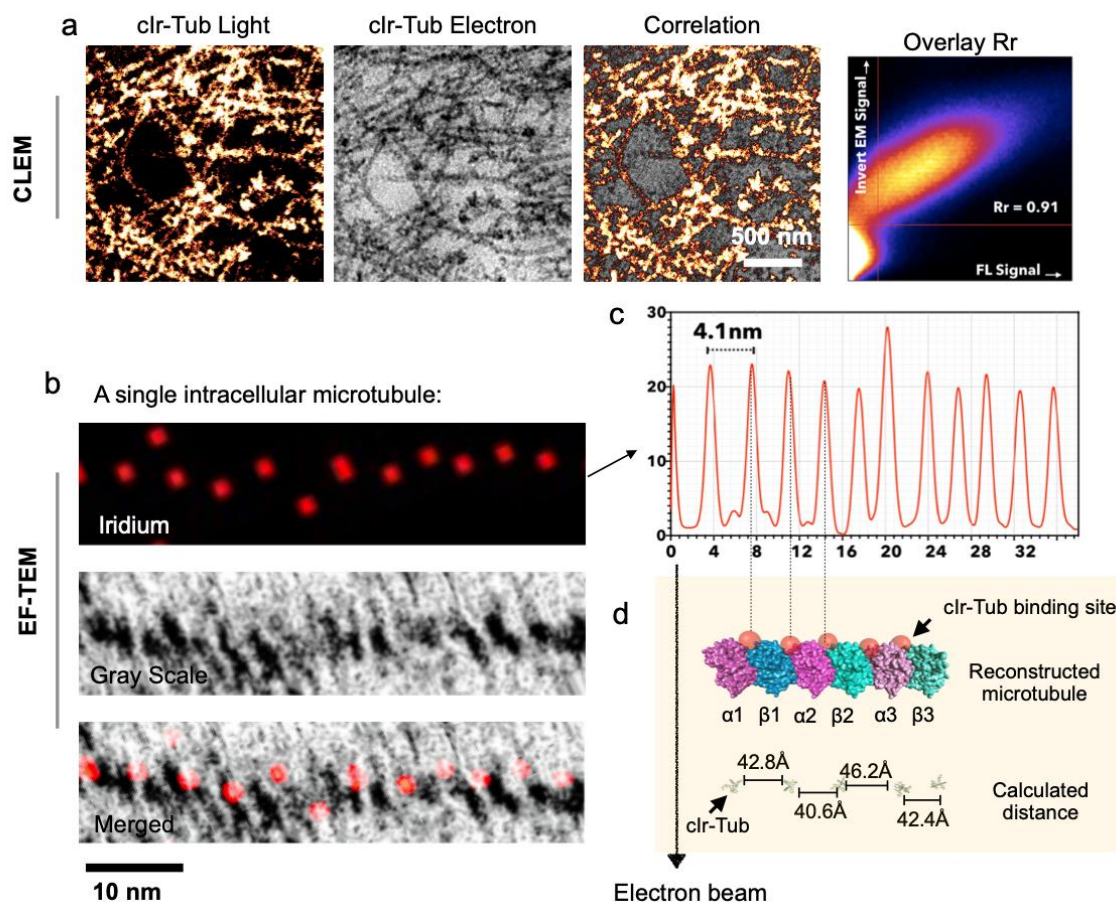
Figure 4: Correlative light and electron microscopy (CLEM) and energy filtered transmission electron microscopy (EF-TEM) imaging. *(a) Correlative super-resolution fluorescent imaging and scanning-transmission electron microscopic image of cIr-Tub labelled microtubules in HepG2 cells. The images obtained using light and EM microscopy were taken from the same site and the co localization scatter plot between fluorescent and inverted electronic microscopic signal shows high correlation with Pearson's coefficient, Rr = 0.91. (b) Conventional TEM image, Iridium elemental mapping and merged images of a single intracellular microtubule. The spacing between the Ir signals in the microtubule is periodic (c) with an average period length of 4.1±0.3 nm. Comparison of this measurement with the distance between the Ir-Tub complex (red sphere) tubulin binding sites as shown in the schemes (d) of the microtubule reconstructed.*

3. Conclusions

In summary, we have designed and synthesized a novel iridium (III) complex, and offered specific intracellular microtubule optical and electron signal correlation that had not previously achieved. The MLCT emission of the cIr-Tub complex 'switched on' upon internalization and facilitating high specificity and sensitivity *in vitro* studies. *In vivo* investigations demonstrated

that the proposed probe enables microtubule tagging and monitoring of cell phases during mitosis. In particular, microtubules were observed under STED nanoscopy by using cIr-Tub at the *in cellulo*, and *ex vivo* level provided ultra-stable and excellent signal-to-noise ratio, resulting in an unprecedented resolution in 3D. Besides, this complex also offered unique, specific contrast for multiple electron microscopic techniques (e.g. CLEM and EF-TEM) along with its optical information. Thus, our approach herein provided a fundamental tool to understand further microtubule dynamics in living systems, as well as a potential targeting vector for therapeutic purposes.

4. Experimental Sections

STED super-resolution image The compound was excited under STED laser (doughnut laser: 595nm), the emission signals were collected using HyD reflected light detectors (RLDs) with 2048*2048 pixel and *100 scanning speed. The STED micrographs were further processed 'deconvolution wizard' function using Huygens Professional software (version: 16.05) under authorized license. The area radiuses were estimated under 0.02 micros with the exclusion of 100 absolute background values. Maximum iterations were 40-time, signal-to-noise ration 20 was applied, with quality threshold 0.05; iteration mode: Optimized; Brick layout: Auto

Correlative light-electron microscopy (CLEM) The ultra-thin (100-120 nm) sections from the above process were moved to ZEISS LSM800 with Airyscan to obtain light microscope data. Electron microscopic imaging was taken under GeminiSEM 500 scanning transmission electron microscopy. To correlative, ZEISS ZEN connect module was chosen to find the same scan region under LM and EM, and ZEISS ZEN shuttle and find module was used merge two images together, the process was described as follow: (1) Set up a connect project in ZEN Blue, and take an overview bright field image of the whole copper grid under LSM800 with the objective of EC Epiplan 5X/0.13. (2) Choose different regions of interest to scan high magnification fluorescent image in the connected project that first set up. (3) Transfer the

copper grid sample to ZEISS GeminiSEM 500 and use the ZEN connect module to open the project data saved in LSM800. (4) Take a large field of view image on GeminiSEM 500 and align those two-overview images. (5) Click the position where the fluorescent image takes; the stage will automatically move to the position where the FL image is. (6) Take the EM image for the sample, and merge the two images by using the ZEISS ZEN shuttle and find module based on the 3-points method.

Chemical analysis by Energy-Filtered TEM The chemical analysis investigation of the specimen was performed using a JEOL JEM-2200FS TEM equipped with a field emission gun (FEG) at 200 kV, and an in-column energy Omega filter. Images were taken at a collection angle of 24.282 mrad. The microscope was used in energy-filtered transmission electron microscopy (EF-TEM) mode in order to perform elemental analysis, and, thus, fine structure imaging. The software used for image acquisition and processing was the Digital Micrograph™ software (version 3.20). Images were recorded using a charge-coupled device (CCD) camera US1000XP from Gatan. The Iridium present in the cells was identified by exciting the atomic O shell (50 eV) with a slit width of 6.0 eV. The 3-window technique was employed. This technique entails two images before the ionization edge and one after. The pre-edge images are used to compute the approximate background contained in the post-edge window. Once the background is determined and removed, the subsequent map displays a signal that is proportional to the element concentration in the sample. The first pre-edge second pre-edge and post-edge energies were 39 eV, 45 eV, and 53 eV respectively. The unfiltered TEM image and the false colour chemical mapping were superimposed using ImageJ software.

Note: All procedures involving animals were approved by and conformed to the guidelines of the Southwest University Animal Care Committee, College of Pharmaceutical Sciences (accreditation number: 001563). We have taken great efforts to reduce the number of animals used in these studies and also taken the effort to reduce animal suffering from pain and discomfort.

5. Acknowledgments

6. References

[1]   W. Kühlbrandt, Science 2014, 343, 1443.

[2]   J. M. Plitzko, B. Schuler, P. Selenko, Current Opinion in Structural Biology 2017, 46, 110; S. Pfeffer, J. Mahamid, Current Opinion in Structural Biology 2018, 52, 111.

[3]   J. Mahamid, S. Pfeffer, M. Schaffer, E. Villa, R. Danev, L. Kuhn Cuellar, F. Förster, A. A. Hyman, J. M. Plitzko, W. Baumeister, Science 2016, 351, 969.

[4]   F. M. Ross, Science 2015, 350, aaa9886.

[5]   M. Fernández-Suárez, A. Y. Ting, Nature Reviews Molecular Cell Biology 2008, 9, 929.

[6]   B. Huang, H. Babcock, X. Zhuang, Cell 2010, 143, 1047.

[7]   G. Vicidomini, A. Schönle, H. Ta, K. Y. Han, G. Moneron, C. Eggeling, S. W. Hell, PLoS One 2013, 8, e54421.

[8]   J. Krijnse Locker, S. L. Schmid, PLoS Biol 2013, 11, e1001639.

[9]   C. Smith, Nature 2012, 492, 293.

[10]   M. Hauser, M. Wojcik, D. Kim, M. Mahmoudi, W. Li, K. Xu, Chemical Reviews 2017, 117, 7428.

[11]   C. J. Peddie, K. Blight, E. Wilson, C. Melia, J. Marrison, R. Carzaniga, M.-C. Domart, P. O'Toole, B. Larijani, L. M. Collinson, Ultramicroscopy 2014, 143, 3; P. de Boer, J. P. Hoogenboom, B. N. G. Giepmans, Nature Methods 2015, 12, 503.

[12]   X. Tian, S. Hussain, C. de Pace, L. Ruiz-Pérez, G. Battaglia, Chemistry – An Asian Journal 2019, 14, 509.

[13]   M. R. Gill, J. Garcia-Lara, S. J. Foster, C. Smythe, G. Battaglia, J. A. Thomas, Nature Chemistry 2009, 1, 662.

[14]   X. Tian, M. R. Gill , I. Cantón, J. A. Thomas, G. Battaglia, ChemBioChem 2011, 12, 548.

[15]   M. R. Gill, D. Cecchin, M. G. Walker, R. S. Mulla, G. Battaglia, C. Smythe, J. A. Thomas, Chemical science 2013, 4, 4512.

[16]   Y. Zhu, M. Zhang, L. Luo, M. R. Gill, C. De Pace, G. Battaglia, Q. Zhang, H. Zhou, J. Wu, Y. Tian, X. Tian, Theranostics 2019, 9, 2158.

[17]   Y. Zheng, M. L. Wong, B. Alberts, T. Mitchison, Nature 1995, 378, 578; D. A. Fletcher, R. D. Mullins, Nature 2010, 463, 485.

[18]   I. Canton, G. Battaglia, Chemical Society Reviews 2012, 41, 2718.

[19]   S. Yogev, R. Cooper, R. Fetter, M. Horowitz, K. Shen, Neuron 2016, 92, 449.

[20]   D. J. Sharp, G. C. Rogers, J. M. Scholey, Nature 2000, 407, 41.

[21]   M. A. Jordan, L. Wilson, Nature Reviews Cancer 2004, 4, 253.

[22]   Y. You, W. Nam, Chemical Society Reviews 2012, 41, 7061.

[23]   C.-Y. Sun, X.-L. Wang, X. Zhang, C. Qin, P. Li, Z.-M. Su, D.-X. Zhu, G.-G. Shan, K.-Z. Shao, H. Wu, J. Li, Nature communications 2013, 4, 2717; K. K.-W. Lo, Accounts of Chemical Research 2015, 48, 2985.

[24]   Q. Zhao, C. Huang, F. Li, Chemical Society Reviews 2011, 40, 2508.

[25]   E. S. Andreiadis, D. Imbert, J. Pécaut, A. Calborean, I. Ciofini, C. Adamo, R.

Demadrille, M. Mazzanti, Inorganic Chemistry 2011, 50, 8197.

[26]   J. Yang, Y. Wang, T. Wang, J. Jiang, C. H. Botting, H. Liu, Q. Chen, J. Yang, J. H.

Naismith, X. Zhu, L. Chen, Nature communications 2016, 7, 12103.

[27]   A. B. Waight, K. Bargsten, S. Doronina, M. O. Steinmetz, D. Sussman, A. E. Prota,

PLoS One 2016, 11, e0160890.

[28]   M. R. Gill, J. A. Thomas, Chemical Society Reviews 2012, 41, 3179.

[29]   R. J. Vasquez, B. Howell, A. M. Yvon, P. Wadsworth, L. Cassimeris, Mol Biol Cell

1997, 8, 973.

[30]   E. A. Nigg, Nature Reviews Cancer 2002, 2, 815.

[31]   L. Y. M. Daddow, Journal of Microscopy 1983, 129, 147.